



HAL
open science

Microstructural and mechanical investigation of the near fusion boundary region in thermally aged 18MND5 / Alloy 52 narrow-gap dissimilar metal weld

A. Akhatova, F. Robaut, M. Verdier, M. Yescas, F. Roch, C. Tassin, Hugo P. van Landeghem

► To cite this version:

A. Akhatova, F. Robaut, M. Verdier, M. Yescas, F. Roch, et al.. Microstructural and mechanical investigation of the near fusion boundary region in thermally aged 18MND5 / Alloy 52 narrow-gap dissimilar metal weld. *Materials Science and Engineering: A*, 2020, 788, pp.139592. 10.1016/j.msea.2020.139592 . hal-02733004

HAL Id: hal-02733004

<https://hal.science/hal-02733004>

Submitted on 2 Jun 2020

HAL is a multi-disciplinary open access archive for the deposit and dissemination of scientific research documents, whether they are published or not. The documents may come from teaching and research institutions in France or abroad, or from public or private research centers.

L'archive ouverte pluridisciplinaire **HAL**, est destinée au dépôt et à la diffusion de documents scientifiques de niveau recherche, publiés ou non, émanant des établissements d'enseignement et de recherche français ou étrangers, des laboratoires publics ou privés.

Microstructural and mechanical investigation of the near fusion boundary region in thermally aged 18MND5 / Alloy 52 narrow-gap dissimilar metal weld

A. Akhatova¹, F. Robaut¹, M. Verdier¹, M. Yescas², F. Roch², C. Tassin¹, H.P. Van Landeghem^{1*}

¹Univ. Grenoble Alpes, CNRS, Grenoble INP, SIMAP, F-38000 Grenoble, France

²Framatome, Materials, Chemistry & Technology Department, 1 Place Jean Millier, 92084 Paris La Défense CEDEX, France

Abstract

Detailed characterization of the near fusion-boundary region of 18MND5 / Alloy 52 dissimilar metal weld joints was performed to investigate the effect of thermal aging on the microstructure and mechanical properties and to quantify the diffusion of carbon into the weld metal. It was shown that the microstructural features of dissimilar metal welds, such as the size of the partially mixed zone in the weld and the adjacency to micro-segregations in the low-alloy steel have an effect on the peak carbon concentration in the enriched region of the weld. Aging conditions (time and temperature) influence the position of this concentration peak in the weld. Those trends were supported by thermodynamic calculations.

Keywords: Dissimilar Metal Weld, Gas Tungsten Arc Welding, Low-Alloy Steel, Nickel-based filler metal, Hardness, Phase transformation

1. Introduction

Dissimilar metal welds (DMWs), such as the joints between the reactor pressure vessel nozzles and safe-ends to the main coolant pipes are key elements in the design and performance of nuclear power plants. High-quality welds are commonly performed by gas tungsten arc welding (GTAW) with Ni-based filler alloys, with or without buttering layers. In these joints, large variations in chemical composition occur at fusion boundaries between the base and filler metals. In particular, the carbon composition changes abruptly from the carbon rich low-alloy steel (LAS) to the carbon lean filler metal. The resulting composition gradient at the LAS/filler metal fusion boundary leads to the diffusion of carbon when it has sufficient mobility. This transfer of carbon is one of the key aspects of the durability of such DMWs [1].

Carbon migration from the heat-affected zone of the steel into the weld metal during post-weld heat treatment (PWHT) is particularly strong with high-Cr filler alloys, such as Alloy

* Corresponding author at SIMaP, 1130 rue de la piscine, BP 75, 38402 Saint Martin d'Hères.
E-mail: hugo.van-landeghem@grenoble-inp.fr

52 [2], [3]. The driving force for carbon migration is the difference in carbon chemical potential between the ferritic LAS and the austenitic nickel-based alloy caused by the variation in chromium and other carbide formers (Nb, Mo) content, as well as the change in structure, across the weld. Experimental results from heat-treated dissimilar metal joints demonstrated the accumulation of carbon close to the fusion boundary on the weld side. It can lead to a carbon build-up of up to about 1.5 wt% C and the formation of Cr-rich precipitates [4], [5] in the first few tens of microns of the weld against the fusion boundary. Accordingly, many authors have reported an increase in the hardness in weld metal next to the fusion boundary [6]–[11]. For instance, Nevasmaa et al. [12] compared two configurations of ferrite–austenite DMWs: one made using a beveled V-groove and Alloy 82/182 filler metal with a buttering layer and one narrow-gap weld using Alloy 52 as a filler metal with no buttering. They found that the applied PWHTs induced different effects on the strength mismatch and fracture behavior of DMWs. In the mock-up with buttering layer, the PWHT was shown to reduce the strength contrast in comparison to the as-welded state, whereas PWHT of narrow-gap GTAW sample accentuated this contrast and resulted in inferior fracture resistance, compared to the as-welded state.

Similarly, the LAS / Alloy 52 fusion boundary was found to be significantly affected by carbon diffusion during aging close to the operation temperature. Sarikka et al. [13] reported that the hardness peak found on the weld side following PWHT tends to level out after 5 000 h and even further after 10 000 h at 400°C. They explained this evolution by the diffusion of carbon from the near-fusion-boundary region deeper into the weld metal. Ahonen et al. [14] found that such aging did lower the fracture resistance of the overall joint but it remained well within specifications. Ahonen et al. [15] believe this drop in mechanical properties is mostly owed to phosphorous segregation.

Therefore, investigating the evolution of the microstructure and the mechanical properties during aging near the LAS / Alloy 52 fusion boundary in narrow-gap DMWs is critical to understand the long-term behavior and performance of such joints in nuclear power plants and is the aim of the present study. Particular attention was paid to the prominent role of carbon distribution in the near-fusion-boundary region and its evolution during aging treatments, using both experimental measurements and thermodynamic calculations. Its impact on local mechanical properties was assessed by nano-indentation.

II. Experimental

A. Materials and processing

The DMW investigated in this paper is an narrow-gap GTAW weld, with Alloy 52 filler metal, between a 18MND5 LAS and a Z2CND18-12 austenitic stainless steel with controlled nitrogen.

The chemical compositions of the 18MND5 LAS, Alloy 52 filler metal and the average composition of the weld far from the fusion boundary used for this work are listed in Table 1.

Table 1. Chemical composition of base materials (in wt%)[16]. For weld metal, Cr, Ni, Fe and Mn contents were measured by electron probe micro-analysis and other elements contents estimated by dilution.

Materials	C	Si	Mn	P	S	Ni	Cr	Mo	Cu	Al	V	Fe	Ti	Ta	Nb
18MND5	0.19	0.23	1.46	0.006	0.006	0.72	0.17	0.48	0.10	0.024	0.003	bal.			
Alloy 52	0.026	0.13	0.25	0.004	0.001	bal.	29.12	0.01	0.01	0.71		10.1	0.51	0.003	0.01
Weld (EPMA)	0.046	0.18	0.429	0.005	0.002	bal.	24.88	0.48	0.03	0.55		21.61	0.45	0.002	0.01

To reduce internal stresses developed during welding the mock-up was subjected to the following PWHT: the whole mock-up was first heated up to 610°C and treated for 6h15 min, then cooled down to 350°C at 40°C/h followed by air cooling to room temperature. It was later subjected to a second similar treatment of 10 h for a total PWHT duration of 16 h at 610°C. Subsequently, coupons cut from the mock-up were aged in air in the temperature range from 350°C to 450°C for various times between 5 000 and 50 000 hours as listed in Table 2.

Table 2. Artificial aging conditions

Sample	Temperature, °C	Aging time, h
E3	-	0
A4	450	5 000
B4	400	5 000
B7	400	30 000
C8	350	50 000

B. Sample preparation and etching

Cross-sections of the 18MND5 / Alloy 52 fusion boundary were cut perpendicularly to the weld beads and polished with SiC abrasive paper down to 4000 grit, followed by polishing using diamond pastes of 3 µm and 1 µm size. In the final step, the samples were polished using an aluminum oxide polishing paste of 0.1 µm grit size and cleaned in ethanol in an ultrasonic cleaner. The ferritic side of the samples was etched using Nital (3% HNO₃ in methanol), the weld side was electrochemically etched in a 10 % chromic acid aqueous solution (10 g CrO₃ in

100 ml H₂O) under a 3 V potential at room temperature. The microstructure of the weld mock-up was observed using an Olympus BX60M light microscope.

Once regions of interest (ROIs) were identified and marked, etching was removed by grinding and polishing again, starting back from 1200 grit SiC to 1 μm diamond. Samples were further finished with 0.1 μm alumina suspension prior to EPMA and nanoindentation analyses.

C. Scanning electron microscopy and energy dispersive spectroscopy

For the pre-selection of comparable ROIs in all samples, evolutions of Fe, Ni and Cr contents in the partially mixed zone of the weld were first semi-quantitatively determined by energy dispersive spectroscopy (EDS). EDS measurements were performed in a JEOL JSM 6400 SEM equipped with a BRUKER AXS SDD detector with a profile step size of 1 μm.

D. Electron probe micro-analysis

Quantitative analysis of Fe, Ni, Cr, Mn and C concentration across the fusion boundary was carried by wavelength dispersive spectroscopy (WDS). Analyses were performed using a Cameca SX50 electron microprobe analyzer (EPMA). Measurements were made every 20 μm in the homogeneous parts of the base and weld metals far from the fusion boundary, and every 4 μm in the near-fusion-boundary region. The measurement was done at 15 kV with beam current of 900 nA for C and Mn and 150 nA for Cr, Ni, Fe. A liquid nitrogen cold trap and a low-pressure jet of oxygen onto the specimen were used to reduce carbon contamination.

Substitutional element contents were measured with LiF monochromators (2d spacing = 0.4 nm). The classic quantitative analytical procedure was taken into account using the ratio of measured intensities of the K α line from the sample and the pure metallic standards. Background intensity was measured and deducted from the peak intensity.

Carbon concentration was measured with a tungsten/silicon multilayer monochromator (2d spacing = 9.5 nm -crystal PC2-). The procedure was based on ISO standard 16592:2012, which postulates a linear relationship between the intensity of the C K α peak and the carbon content in the probed volume (in wt%). The samples used as references were electrolytic iron and various fully martensitic steels with carbon contents varying from 0.0006 to 0.99 wt%.

E. Nano-indentation

Nano-indentation tests were performed to map hardness across the fusion boundary with a high spatial resolution (typically 2 μm pitch), using an MTS XP machine equipped with a diamond Berkovich indenter. Two mapping patterns were used. The first is a coarse matrix (2 × 28 points, 25 μm pitch) with a final indentation depth of 400 nm. The second is a finer matrix (5 × 25 points, 2.5 μm pitch) with a 100 nm final depth, centered over the fusion

boundary. Hardness and elastic modulus were continuously determined along the indentation depth using the standard Oliver and Pharr method [17] and superimposed 2 nm oscillations at 45 Hz.

F. Transmission electron microscopy

Transmission electron microscopy (TEM) specimens were prepared using focused ion beam (FIB) lift-out in a dual beam microscope to control their locations within the determined ROIs. Before observation, the specimens were cleaned in a Gatan Solarus plasma cleaner for 4 min in O₂/H₂ mixture followed by for 4 min in Ar/H₂. The specimens were observed in a JEOL 2100F TEM operated at 200 kV.

G. Thermodynamic calculations

Thermodynamic calculations were performed using the DICTRA (Diffusion Controlled TRAnsfOrmations) package in Thermo-Calc® software (Solna, Sweden) together with the TCFE9 and MOB2 databases. This tool allows the prediction of atomic diffusion in one dimension resulting from chemical potential gradients. The DMW was treated using the cell concept in DICTRA, each material (LAS and weld) being placed in a separate cell. In the calculations, the program iterates until it detects that the chemical potentials at the cell boundary conform to the mass balance. The phases selected for the computations were the matrix phases (BCC ferrite for the LAS and FCC austenite for the weld) and several carbides (cementite M₃C, M₂₃C₆, M₇C₃, M₂C and M₃C₂). Elements considered were C, Cr, Fe, Ni, Mn, Mo, Si and input composition profiles were those measured by EPMA (C, Cr, Fe, Ni, Mn) on the PWHT sample or calculated by dilution (Mo, Si) based on the Ni content. Thermal aging treatments were reduced to their holding temperature and time, neglecting the heating and cooling parts.

The WDS-measured profiles of C, Cr, Fe, Ni and Mn were fitted in order to the get smooth profile with geometrical series of step (initial step = 1 μm). The experimental profiles with their fitting curves are presented in Figure 1. Fe, Cr, Ni and Mn concentration profiles are fitted according to,

$$F(x_i) = F_0 - A * erf(B * (C - x_i)) \quad (1)$$

Where x_i is a distance, A, B, C are the fit parameters and F_0 is the fixed concentration of atoms at the left end of the couple (in the LAS). C profile was fitted with a set of exponential functions at the intervals [-800:0], [0:16], [16:23], [23:400] μm.

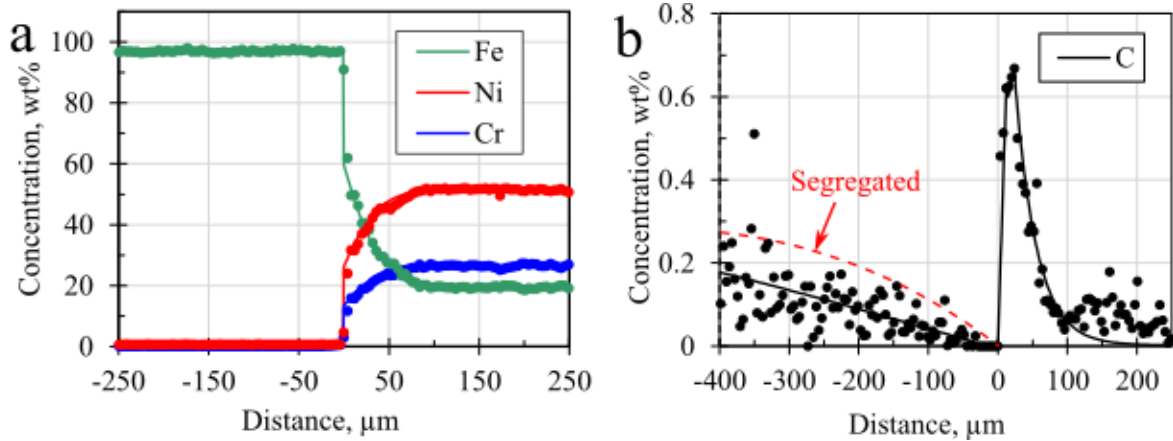


Figure 1: Experimental concentration profiles of (a) iron, nickel, chromium and (b) carbon concentration as a function of the distance from the interface (610°C, 16 h) given by symbols. The lines represent the corresponding fitted profiles used as the input of the simulation.

III. Results

A. Evolution of composition and microstructure through the weld

Figure 2 shows a macrograph of the cross-section of the mock-up after PWHT, revealing the different zones of DMW, including the heat-affected zone of the LAS about 2.5 mm wide. The first weld bead in contact with the LAS was taken as a starting point for their numbering.



Figure 2: Optical macrograph of the dissimilar metal weld mock-up after post-weld heat treatment. Numbering of weld beads was started ($N=0$) at the first bead in contact with LAS, as shown by the dotted line.

Figure 3 shows optical micrographs of the weld joint microstructure after PWHT. The LAS side far from the fusion boundary displays the typical bainitic microstructure of 18MND5 steel grade. Close to the fusion boundary, it is replaced by ferrite with a grain size of a few tens of micrometers, as a result of carbon diffusion from the LAS side to the weld side that notably leads to the dissolution of cementite, as illustrated in Figure 3b. The main part of the weld exhibits a cellular / dendritic structure with large grains elongated, millimeter-sized in the solidification direction, perpendicular to the solid-liquid interface, and a few hundreds of micrometer wide in the transversal section. A white layer where no microstructure is revealed by etching can be observed along the fusion boundary on the weld side: it corresponds to a thin layer where the local solidification conditions lead to plane front growth [18].

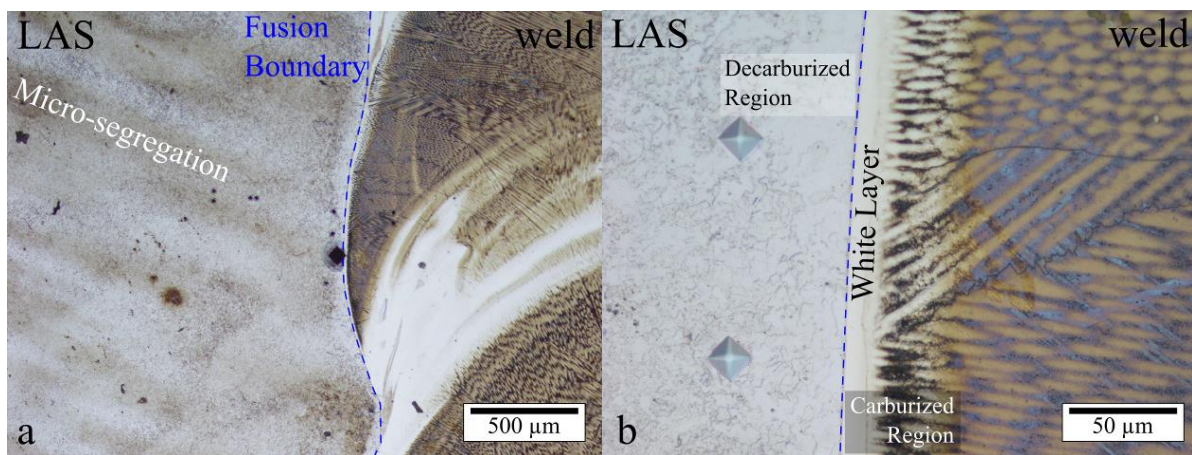


Figure 3: a) Optical micrograph of 18MND5/Inconel 52 fusion boundary cross section in a sample aged for 5 000 h at 400°C following post-weld heat treatment. b) Close-up of the near-fusion-boundary region at the center of a).

Dark-etched bands on the LAS side are related to the carbon micro-segregation zones and are also known as ghost lines [15]. Micro-segregation is a known phenomenon that takes place during the casting of large ingots [19]. It is a material heterogeneity in the form of a chemical gradient that deviates from the nominal composition and may locally exceed specification limits. Microprobe analysis has shown dark-etched bands to be enriched in solute elements such as C, Cr, Ni and Mn, as detailed in Table 3.

A similar result was reported by Naudin in 18MND5 LAS [20] where it was found that A-segregations were enriched in solute elements and impurities as shown in Table 3. The similarity between average A-segregations and micro-segregations was already noted by Andrieu [21] who considered them to behave similarly in terms of phase transformations and mechanical properties. Carbon concentration in segregated zone was found to be significantly greater than bulk content, about 1.8 times higher on average. Consequently, the influence of segregated zones on the carbon concentration in the weld will be examined in the present article.

Table 3. Chemical composition of segregated and non-segregated zones in 18MND5 measured by EPMA in sample A4, compared to composition measurements in segregated zones in 18MND5 reported by Naudin [20].

Source	wt%	C	Cr	Ni	Mn
Present work	Bulk composition of LAS	0.19	0.17	0.72	1.46
	Average concentration in segregated zone	0.36 ± 0.07	0.20 ± 0.01	0.82 ± 0.05	1.72 ± 0.06
	Average concentration in non-segregated zone	0.17 ± 0.05	0.17 ± 0.02	0.72 ± 0.03	1.48 ± 0.06
Naudin [20]	Bulk composition of LAS	0.16	0.19	0.70	1.35
	Average concentration in segregated zone	0.25	0.22	0.86	1.88
	Maximum concentration in segregated zone	0.40	0.4	1.0	2.3

As usually observed in DMWs and consistently with the chemical compositions given in Table 1, a composition gradient exists between the LAS and the weld metal. Figure 4 shows a distinct intermediate zone with substitutional content gradients, characteristic of a partially mixed zone. From the LAS to the weld metal, Fe, Ni and Cr contents change abruptly across the fusion boundary, then more gradually in the partially mixed zone, before they finally become constant in the fully mixed zone. It is important to note that this abrupt change was used throughout this study to determine the position of the fusion boundary in composition profiles. Given the 4 μm step used for those profiles, the distances to the fusion boundary are given $\pm 2 \mu\text{m}$. Regarding the overall aspect of carbon profiles, carbon content is almost constant far from the fusion boundary, up until within about 100 μm , where it starts decreasing due to the carbon transport occurring from the LAS to weld during the various thermal treatments, including PWHT. The carbon transferred into the metal is then accumulated in a region right after the fusion boundary. The size of this region and the amount of carbon involved depend on the total thermal paths, as detailed further. Past this carbon-rich region, the weld metal shows very low carbon content. It sometimes spikes over a single point in the profiles, which is due to the presence of sparse micron-sized titanium carbides, likely formed during solidification given their extremely low solubility.

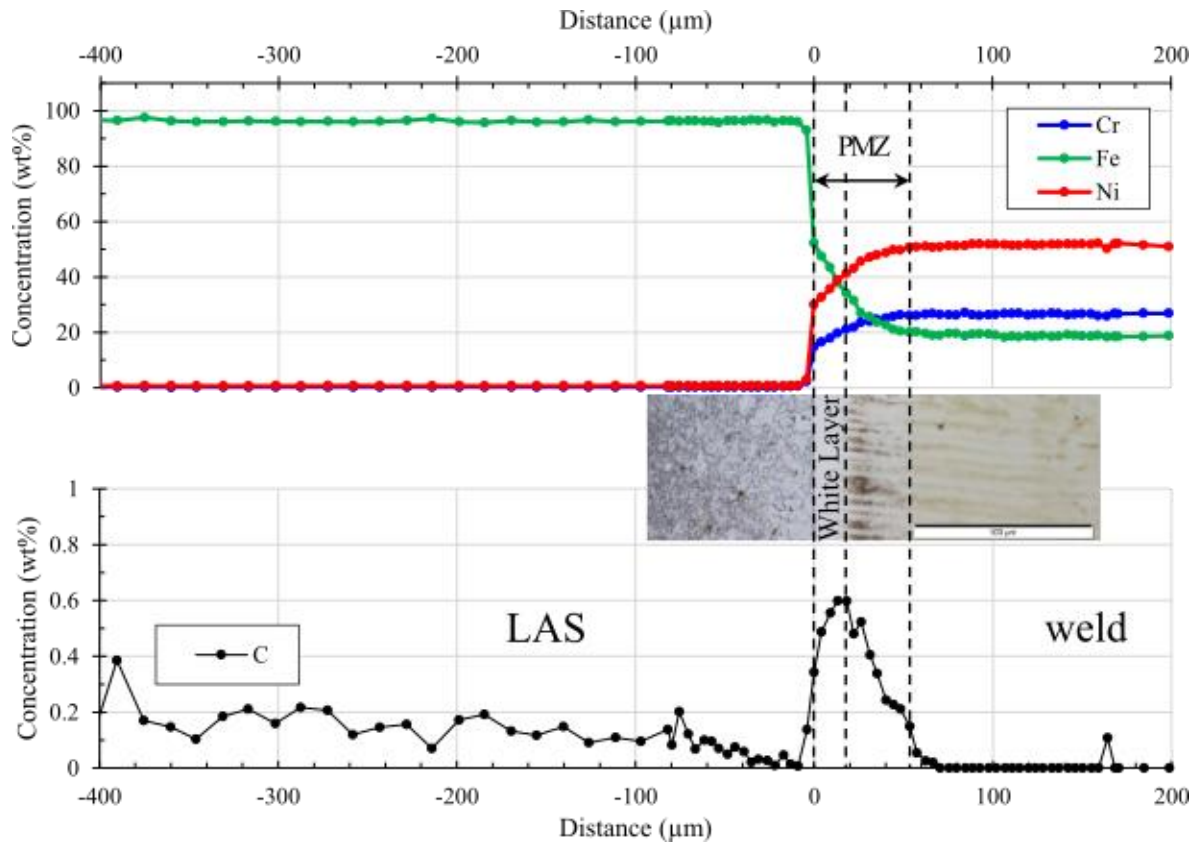


Figure 4: Composition profiles measured across the fusion boundary between the 18MND5 low alloy steel (left side) and weld metal (right side) in sample A4, aged for 5 000 h at 450°C following post-weld heat treatment.

TEM observation of the microstructure at the carbon peak revealed an abundant precipitation of nano-sized elongated particles, as illustrated by Figure 5. These particles were found in all samples in varying amounts. Electron diffraction confirmed the presence of a secondary phase by showing a lattice of dimmer diffracted beams in addition to those of austenite. They can be indexed as $M_{23}C_6$, a chromium rich carbide with a FCC structure in a cube-on-cube orientation relationship with the matrix and a lattice parameter ($\approx 10.6 \text{ \AA}$) approximately 3 times as large as that of the matrix ($\approx 3.6 \text{ \AA}$) [22].

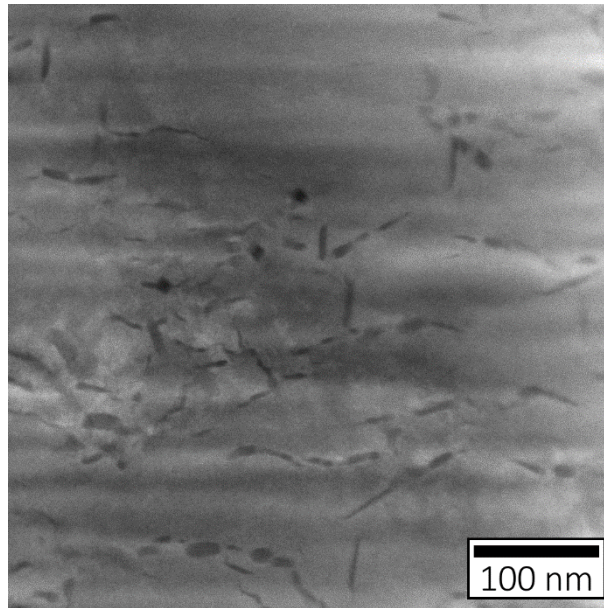


Figure 5: Scanning electron transmission micrograph of region 25S1 in C8 at the carbon concentration peak, 16 μ m away from the fusion boundary. The horizontal variations in contrast are an artifact of focused ion beam preparation of the specimens.

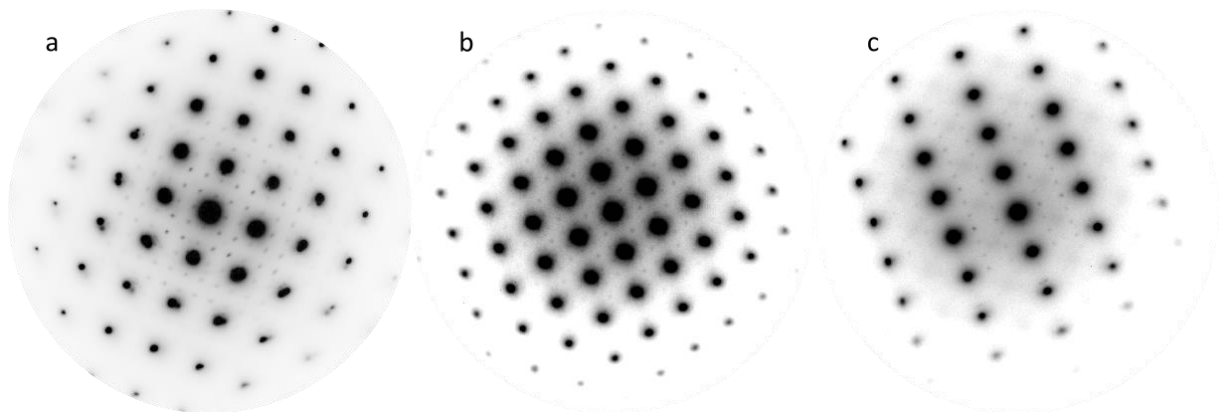


Figure 6: Selected area electron diffraction patterns recorded from the same specimen as Figure 5 in a) [001] $_{\gamma}$, b) [011] $_{\gamma}$ and c) [112] $_{\gamma}$ zone axes. The large, intense reflections are produced by the austenitic matrix. The smaller, dimmer ones match the crystal structure of $M_{23}C_6$ carbide in cube-on-cube orientation relationship with austenite.

B. Evolution of carbon distribution and hardness during aging

Table 4 summarizes the fusion boundary characteristic data: white layer and partially mixed zone widths, corresponding measured peak values of carbon and hardness in the weld. The extent of the white layer is determined visually and that of the partially mixed zone is chosen as the distance after which Ni content is greater than 98 % of its plateau value. The profile index corresponds to the number of the welding bead, N and S indicate non-segregated and segregated zones, and the last number is used to separate two profiles close together in the same welding bead. The collection of measurements found in Table 4 highlights the strong heterogeneity that occurs along the same fusion boundary, which is common in narrow-gap

GTAW DMWs. To finely characterize the microstructure in the near-fusion-boundary region, local scale characterization techniques were used such as EPMA or nano-indentation and, in an effort to capture this heterogeneity, multiple measurements were distributed along the fusion boundary. In what follows, this aspect must be kept in mind when assessing the agreement across different results.

Table 4. Summary of fusion boundary characteristics

Sample	Profile	White Layer size, μm	Partially Mixed Zone size, μm	Carbon peak		Hardness peak	
				Value, wt%	Position, μm	Value, GPa	Position, μm
E3 Post-Weld Heat-Treated (PWHT)	17N	12	91	0.79	22.5	-	
	18N1	15	88	0.67	20	6.5 \pm 0.3	18
	18N2	15	93	0.66	20	-	
C8 PWHT + 350°C, 50 000 h	24N	18	92	0.72	18	6.8 \pm 0.2	11
	25S1	17	56	0.88	16	8.6 \pm 0.5	12
	25S2	19	85	1.31	14	-	
A4 PWHT + 450°C, 5000 h	15N	17	84	0.60	13	7.2 \pm 0.4	17.5
	15S	17	62	0.82	13	8.1 \pm 0.1	15
	16N	14	52	1.21	13.5	-	
	16S	14	50	1.43	9	-	
B4 PWHT + 400°C, 5000 h	22S	14	86	1.93	8	9.9 \pm 0.1	9
	23N	16	67	1.1	9	5.7 \pm 0.1	6-26
	24N	14	54	1.37	8	-	
B7 PWHT + 400°C, 30 000 h	20S	18	45	1.16	18.5	8.1 \pm 0.9	20
	20N	16	41	1.34	19	7.7 \pm 0.2	20

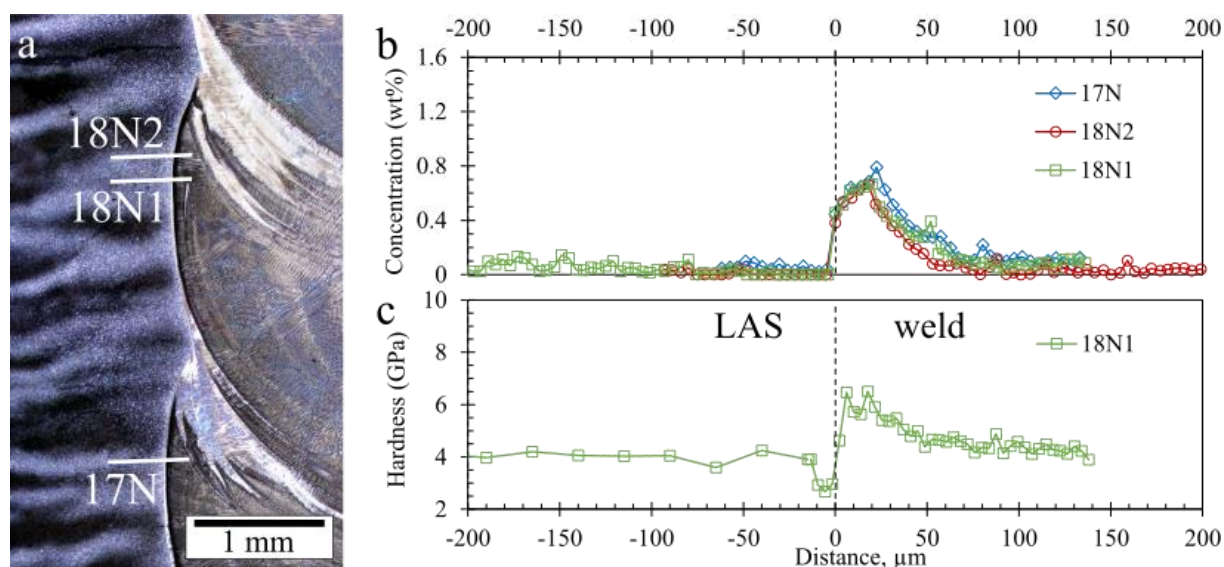


Figure 7. Analysis of post-weld heat-treated specimen E3: (a) light micrograph with profile locations, (b) carbon concentration profiles across the fusion boundary (steel on the left and weld on the right), (c) nano-hardness profile across the fusion boundary (steel on the left and weld on the right)

Figure 7a shows the locations of three ROIs in the PWHT sample E3. All three carbon composition profiles shown in Figure 7b were recorded in non-segregated zones in the LAS

and have similar widths of white layer and partially mixed zone as seen in Table 4. On the LAS side, carbon concentration is low compared to the bulk content of the material. That is related to the proximity with non-segregated bands, which are carbon-lean compared to segregated bands as mentioned above. The nano-hardness profile recorded in ROI 18N1 is presented in Figure 7c. It reveals that hardness is very homogeneous in the LAS up until a few tens of microns from the fusion boundary, where it starts dropping. Past the fusion boundary, the hardness increases higher than the hardness level recorded further in the weld. The extent of this zone of elevated hardness matches that of the zone of elevated carbon content.

In Figure 8, similar analyses are presented for sample B4, aged 5 000 h at 400°C following PWHT. It can be observed here that the ROI near a micro-segregation in the LAS, noted S, show a higher peak carbon content than regions away from them, noted N. This observation can be generalized to the other samples as can be seen from Table 4. The overall size of the carbon-enriched zone remains similar ($\approx 60 \mu\text{m}$) to the PWHT state in all ROIs. In terms of hardness, it is slightly higher on the LAS side in micro-segregations, which is expected given the slightly higher carbon content. On the weld side, the hardness peak is also higher near micro-segregations, showing here again a strong correlation between hardness and local carbon content. This correlation is also seen in the other samples listed in Table 4.

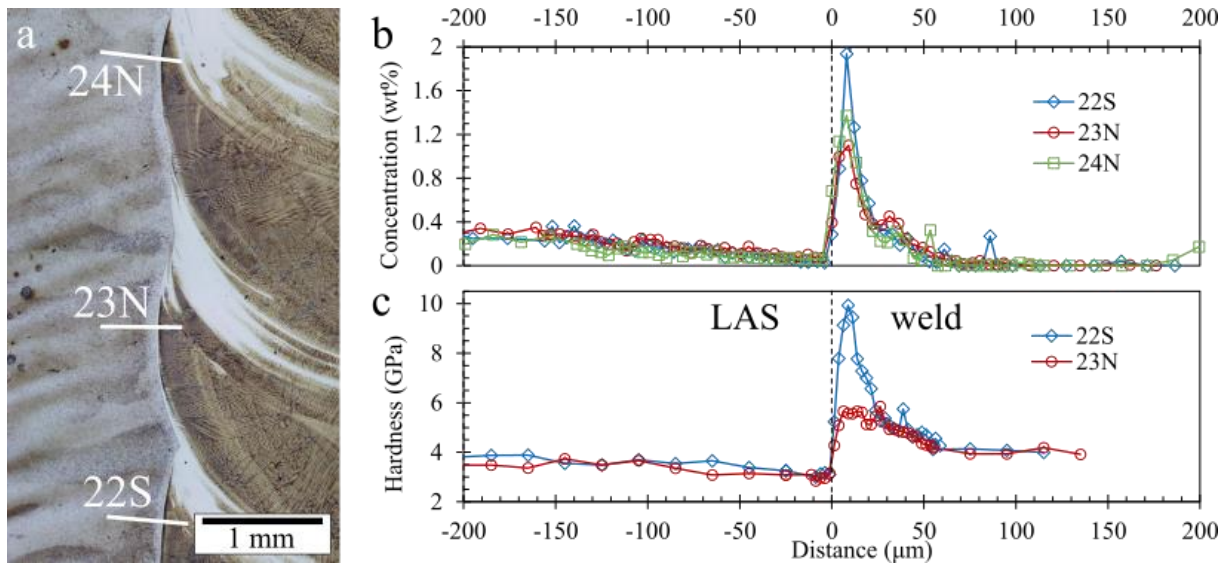


Figure 8: Analysis of specimen B4, aged for 5 000 h at 400°C following post-weld heat-treatment: (a) micrograph with profile locations, (b) carbon concentration profiles across the fusion boundary (steel on the left and weld on the right), (c) nanohardness profiles across the fusion boundary (steel on the left and weld on the right).

C. Modelling chemical evolution across dissimilar interfaces

DICTRA simulation was carried out based on experimental data from profile 18N1 recorded on PWHT sample E3 and shown in Figure 7. It passes through a non-segregated zone.

As shown in Table 3, it was found that the average concentration of carbon in segregated and non-segregated zones 0.36 ± 0.07 and 0.17 ± 0.05 wt%, respectively. To investigate the effect of LAS carbon content on the evolution of the peak carbon content after aging, a carbon profile with higher carbon concentration (0.3 wt% at the maximum) was assumed on the LAS side to model segregated, carbon-rich bands, as plotted in Figure 1b.

The diffusion simulations consisted in isothermal holds corresponding to the experimental aging treatments, i.e. 350°C during 50 000 h, 400°C during 30 000 h, and 450°C during 5 000 h. The simulation results in Figure 9 show that carbon is predicted to diffuse from the LAS side to the weld side, since the weld has both a higher chromium concentration and an fcc structure, which result in a lower carbon activity.

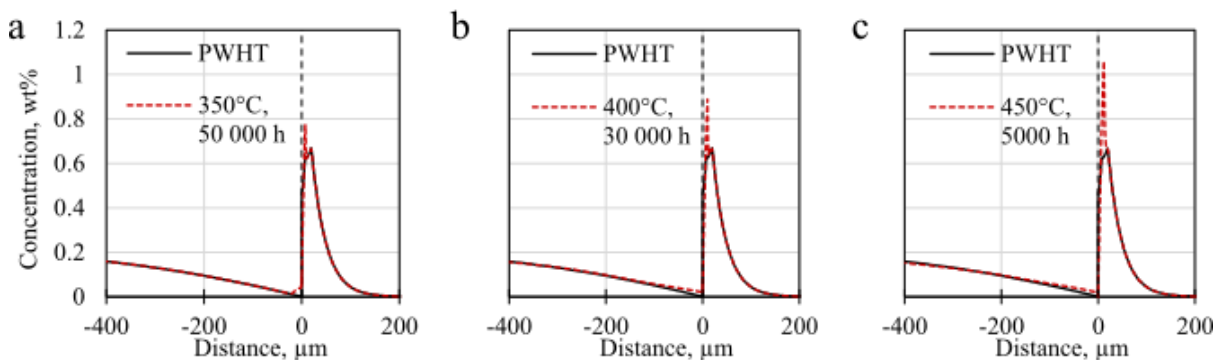


Figure 9: Simulated carbon concentration profiles after (a) 50 000 h at 350°C, (b) 30 000 h at 400°C and (c) 5 000 h at 450°C.

This diffusion has resulted in minor increase of carbon in the carbon depleted zone (CDZ) just before the fusion boundary, and a carbon peak increase of $\approx 22\%$, $\approx 33\%$ and $\approx 45\%$ after aging at 350°C during 50 000 h, at 400°C during 30 000 h, and at 450°C during 5 000 h, respectively. This increase takes place by the formation of a new carbon peak closer to the fusion boundary than the original one. The position of this peak changed across the different simulation going from 7 μm after 50 000 h at 350°C to 11 μm after 5 000 h at 450°C.

The effect of carbon content in the steel was investigated by simulating the thermal treatment at 450°C during 5 000 h with two different starting carbon profiles on the LAS side as illustrated by Figure 10. As expected, the carbon peak is higher in the austenite adjacent to segregated zone. However, the difference is not as pronounced as in the experimental S and N profiles.

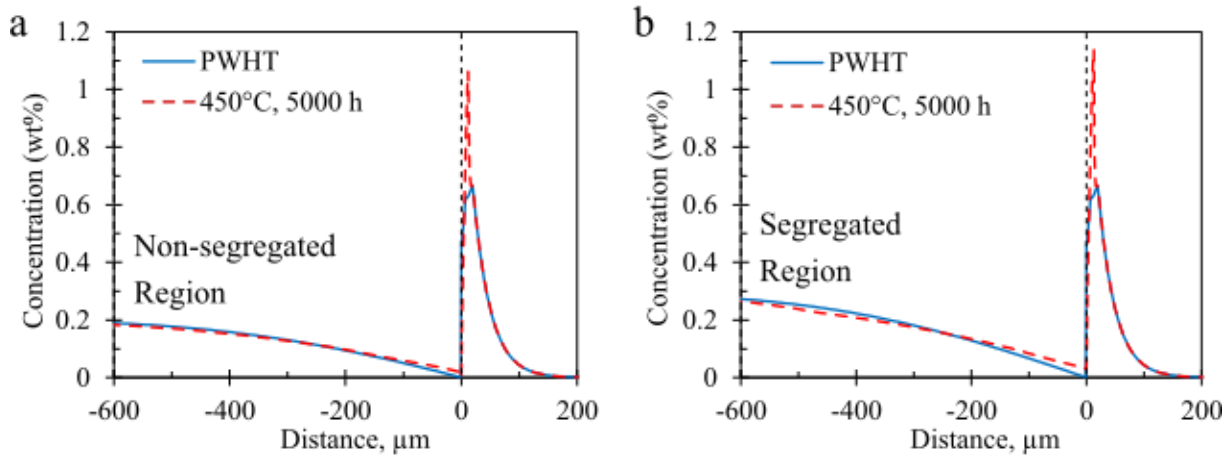


Figure 10: Simulated carbon concentration profiles near (a) non-segregated and (b) segregated zones after 5 000 h at 450°C.

IV. Discussion

A. Representativeness of ROIs

It is evident from the analytical data presented in this paper that the local composition profiles across the interface vary greatly along the fusion boundary. Since it is desirable to maintain high spatial resolution perpendicularly to the fusion boundary, it is challenging from a practical standpoint to acquire a representative dataset. This limitation imposes to select a restricted number of ROIs in each sample; therefore, it is important to select comparable ROIs across all samples. Consequently, it would be desirable to be able to select such ROIs based on a microstructural feature. For this reason, the first criterion utilized was the size and morphology of the white layer. The study focused on regions where the boundaries of the fusion boundary and the white layer are parallel because it represents the larger fraction of the fusion boundary length and because these regions are less prone to abrupt changes in the out-of-plane direction. However, it can be observed in Table 4 that the size of the white layer, chosen here to be around 15 μm , does not correlate well with the size of the partially mixed zone, which is a direct characteristic of the local composition profile. This requires additional measurements after the initial ROI selection step.

Consequently, EDS substitutional composition profiles were recorded across all ROIs to ensure that they feature comparable local substitutional concentration fields. Since those fields will not be affected by thermal aging, the evolution of the microstructure, interstitial content, and mechanical properties can be investigated as a function of their environment of substitutional elements.

B. Carbon mass transport

There exists a gradient of carbon chemical potential across the 18MND5 / alloy 52 fusion boundary that leads to the diffusion of the carbon contained in the LAS to the weld side of the fusion boundary when its mobility is sufficient. This carbon potential gradient is related to the composition gradient of all solutes, in particular chromium, which has a strong attractive interaction with carbon. Given the high solute contents on the weld side, this carbon transfer also results in an intense precipitation of carbides on the weld side, mostly chromium rich $M_{23}C_6$ as evidenced by Figure 5 and Figure 6. The carbon atoms involved in such a precipitation reaction no longer participate to diffusion, leading to interconnected diffusion and precipitation kinetics.

Carbon analysis shows that carbon diffusion from the LAS into the weld occurs already during welding and PWHT, the maximum carbon peak value measured in the weld after PWHT being 0.79 wt%, measured in a zone adjacent to non-segregated band in LAS. The width of the carburized zone is about 60 μm .

Given the data shown in Table 4, it can be seen that the position of the carbon peak is closely related to its aging conditions in all ROIs. The carbon peak is, in all aged conditions, closer to the fusion boundary than right after PWHT. However, the carburized depth in the weld seems to be little affected, if at all, as seen in Figure 8. Additionally, it seems that there exists a shoulder after the peak in most ROIs of aged samples whereas this feature is absent in the PWHT sample. This is consistent with the carbon transport mechanism revealed by the numerical simulation. It can be seen Figure 9 that during aging, the modification of the carbon profile occurs by creation of a new carbon content peak, higher than the one obtained after PWHT and closer to the fusion boundary. In the rest of the carburized region, the profile remains almost identical. The distance from the fusion boundary of the peak formed during aging was systematically underestimated. This is also possibly due to the assumption of the model used here that assumes that phase transformations are instantaneous and thus that precipitate fractions are always at equilibrium. Carbon captured in carbides is no longer mobile and is thus trapped much closer to the fusion boundary than if part of it remained longer in solid solution due to finite reaction kinetics. This suggests that precipitation kinetics should be accounted for in order to quantitatively model carbon transport in this DMW.

The maximum values reached at the carbon concentration peaks are quite scattered. One possible explanation for this disagreement is the local variations of carbon in the LAS. It can be noticed from Table 4 that ROIs adjacent to dark segregation bands present a larger carbon peak. The larger carbon content in those bands on the LAS leads to a steeper chemical potential

gradient across the fusion boundary and the partially mixed zone, and a larger mass transfer during aging. Results from the simulation showed a reasonable agreement with the peak content found in non-segregated ROIs. Nevertheless, simply assuming a base carbon level in the LAS as the segregated content from [20] did not reproduce the peak content found in segregated ROIs. It is thought that the original peak of the PWHT condition plays a role as well. This peak is likely to be higher in segregated regions but no measurement in such regions could be successfully carried out during the present study, thus this hypothesis remains to be confirmed.

It should also be reminded here that the gradient of carbon chemical potential is not only affected by the local carbon concentration but also by other elements as well and in particular by chromium. Figure 11 shows the Cr profiles across the fusion boundary for ROIs that are all adjacent to non-segregated bands in the LAS, where carbon content is lower. From these profiles, it can be observed that shallower Cr gradients are associated to lower carbon peaks. Chromium is known to decrease the chemical potential of carbon and thus, a shallower Cr content gradient leads to a shallower C chemical potential gradient. This, in turn, results in a lower mass transfer and smaller concentration peak after identical aging.

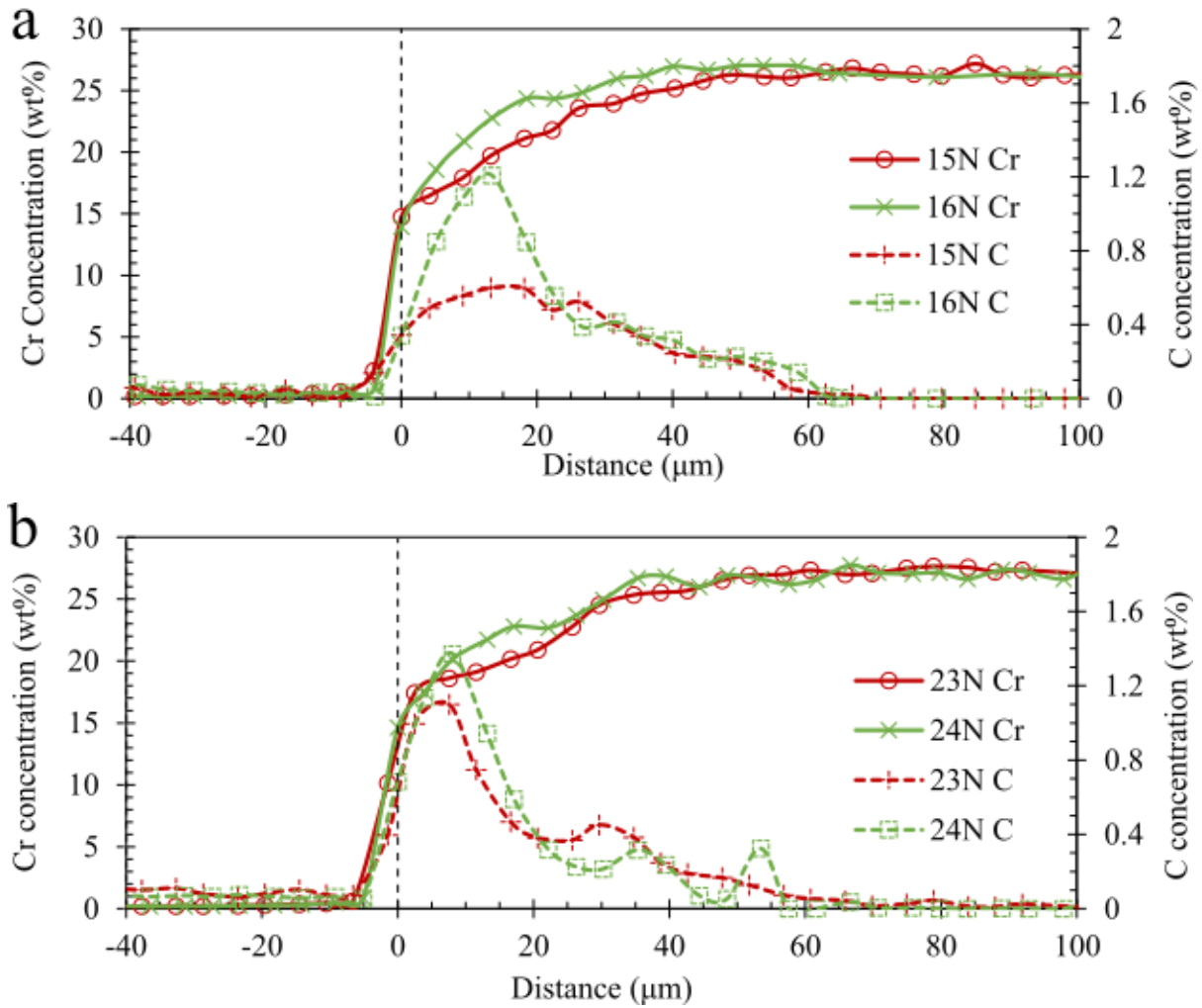


Figure 11: Cr profiles across the fusion boundary (steel in the left and weld in the right) adjacent to the non-segregated zone of LAS in (a) sample A4 (450°C, 5 000 h), (b) sample B4 (400°C, 5 000 h).

C. Evolution of microstructure and mechanical properties

Nano-hardness measurements revealed substantial variations of the mechanical properties across the fusion boundary in all conditions. On the LAS side, far from the fusion boundary, a hardness of about 4 GPa was recorded and is consistent with tempered bainite. Within 150 μm from the fusion boundary, the value gradually drops to about 3 GPa due to carbon depletion. Past the fusion boundary into the weld, the hardness increases sharply to a peak whose maximum and location depend on the aging condition. Further away, it decreases to between 4 and 5 GPa

The data set in Table 4 reveals a close correlation between peak carbon concentration and peak hardness. In fact, Figure 7 and Figure 8 show that the shape of hardness profiles is closely similar to the carbon concentration profile.

Peak hardness after aging can be extremely high, close to 10 GPa compared to a base line of about 4.5 GPa in the weld metal. It is expected that carbon diffusion hardens the austenitic weld metal through solid solution strengthening, but that sole mechanism seems insufficient for such elevated hardness levels. Those hardness levels can be explained by the presence of the nano-precipitates shown in Figure 5. Those precipitates were shown to be $M_{23}C_6$ carbides, the presence of which is predicted by thermodynamic calculations throughout the PMZ. Those calculations also predict the presence of M_7C_3 carbides in the first few microns past the fusion boundary, which was not observed here.

V. Conclusion

In summary, the experimental results highlight the challenge of fine scale characterization of the near-fusion-boundary region in narrow-gap DMWs. The inhomogeneity inherent to the welding process calls for careful selection of multiple ROIs in the same welded joint. This work demonstrates the importance in this process of white layer and partially mixed zone thicknesses as well as the adjacency to segregated/non-segregated zone on the LAS side. The following conclusions can be drawn from the study.

1. During welding and PWHT, carbon diffuses from the steel heat-affected zone and leads to the carbon enrichment in a narrow zone on the weld side of the fusion boundary. EPMA measurements showed the peak value of carbon to be 0.6 ± 0.1 wt% following PWHT. Subsequent thermal aging in the 350°C - 450°C range increases the peak value of carbon up to 1.93 wt% (400°C , 5 000 h).

2. The average carbon concentrations in segregated and non-segregated zones in steel are 0.36 ± 0.07 and 0.17 ± 0.05 wt%, respectively. The carbon peak values near fusion boundaries adjacent to segregated zones are on average ≈ 30 % higher than in zones near non-segregated bands.

3. The carbon peak value and its position relative to the fusion boundary coincide well with the nanohardness peak. This correspondence confirms that the high hardness in a narrow zone on the weld side of the fusion boundary is a result of the increased carbon content in the weld and the carbide precipitation it leads to.

4. The position of the carbon peak with respect to the fusion boundary seems to be mostly controlled by the aging condition. This causes the carbon peak value to be lower in wider partially mixed zone for a given aging condition, since the shallower Cr concentration gradient and the associated shallower carbon chemical potential gradient lead to a smaller carbon transfer to the weld.

5. Thermodynamic calculations showed that the amount of carbon transferred across the fusion boundary increases with aging temperature and time, in a given substitutional composition gradient.

6. Thermodynamic calculations revealed the mechanism involved in the evolution of the carbon profile during aging, with the formation of a new peak close to the fusion boundary that progresses and overtakes the initial peak formed during welding and PWHT. Such calculations showed a reasonable ability to predict the peak value. Its distance from the fusion boundary was however, systematically underestimated.

7. Thermodynamic calculations predicted the presence of chromium rich $M_{23}C_6$ carbides throughout the PMZ, which was experimentally confirmed by electron diffraction in TEM. They also predict the presence of M_7C_3 carbides close to the fusion boundary, which was not observed here.

8. The effect of carbon content in the steel was investigated by simulation of thermal aging at 450°C during 5 000 h. The predicted carbon peak value did increase with the carbon content in LAS but not as much as experimentally observed. Further work is still necessary to quantify the effect of dark bands on carbon transfer across the fusion boundary, starting from the as-welded state.

VI. Acknowledgement

Part of this work was performed with the support of the Center of Excellence of Multifunctional Architected Materials “CEMAM” No. AN-10-LABX-44-01 funded by the “Investment for the Future” Program operated by the National Research Agency (ANR).

VII. Data availability

The raw and processed data required to reproduce these findings cannot be shared at this time as the data also forms part of an ongoing study.

VIII. Bibliography

- [1] G. J. Brentrup and J. N. Dupont, ‘Fabrication and Characterization of Graded Transition Joints for Welding Dissimilar Alloys’, *Weld. J.*, vol. 92, no. 3, pp. 72s–79s, Mar. 2013.
- [2] H. Hänninen *et al.*, ‘Dissimilar metal weld joints and their performance in nuclear power plant and oil refinery conditions’, p. 212.
- [3] R. Mougnot, T. Sarikka, A. Brederholm, T. Saukkonen, and H. Hänninen, ‘Characterization of a Ni-base NG-DMW weld of modern PWR’, p. 15, 2014.

- [4] J. N. DuPont, ‘Microstructural evolution and high temperature failure of ferritic to austenitic dissimilar welds’, *Int. Mater. Rev.*, vol. 57, no. 4, pp. 208–234, Jul. 2012, doi: 10.1179/1743280412Y.0000000006.
- [5] M. L. Huang and L. Wang, ‘Carbon migration in 5Cr-0.5Mo/21Cr-12Ni dissimilar metal welds’, *Metall. Mater. Trans. A*, vol. 29, no. 12, pp. 3037–3046, Dec. 1998, doi: 10.1007/s11661-998-0211-1.
- [6] Z. R. Chen, Y. H. Lu, X. F. Ding, and T. Shoji, ‘Microstructural and hardness investigations on a dissimilar metal weld between low alloy steel and Alloy 82 weld metal’, *Mater. Charact.*, vol. 121, pp. 166–174, Nov. 2016, doi: 10.1016/j.matchar.2016.09.033.
- [7] K. J. Choi, S. C. Yoo, T. Kim, C. B. Bahn, and J. H. Kim, ‘Effects of aging temperature on microstructural evolution at dissimilar metal weld interfaces’, *J. Nucl. Mater.*, vol. 462, pp. 54–63, Jul. 2015, doi: 10.1016/j.jnucmat.2015.03.044.
- [8] T. Sarikka *et al.*, ‘Effect of mechanical mismatch on fracture mechanical behavior of SA 508 – Alloy 52 narrow gap dissimilar metal weld’, *Int. J. Press. Vessels Pip.*, vol. 157, pp. 30–42, Nov. 2017, doi: 10.1016/j.ijpvp.2017.08.003.
- [9] B. A. Soares, ‘Characterization of the dissimilar welding - Austenitic stainless steel with filler metal of the nickel alloy’, presented at the International Nuclear Atlantic Conference, Santos, SP, Brazil, Oct. 2007.
- [10] ‘VTT Technology 333: Thermal ageing and mechanical performance of narrow-gap dissimilar metal welds’, p. 193.
- [11] W. Wang, Y. Lu, X. Ding, and T. Shoji, ‘Microstructures and microhardness at fusion boundary of 316 stainless steel/Inconel 182 dissimilar welding’, *Mater. Charact.*, vol. 107, pp. 255–261, Sep. 2015, doi: 10.1016/j.matchar.2015.07.018.
- [12] P. Nevasmaa *et al.*, ‘Fracture mechanical characterisation of ferrite-austenite dissimilar metal welds (DMWs) for elevated temperature service in view of metallurgical mismatch’, presented at the Baltica IX, Helsinki-Stockholm, Jun. 2013, p. 23.
- [13] T. Sarikka *et al.*, ‘Microstructural Characterization of Alloy 52 Narrow-Gap Dissimilar Metal Weld After Aging’, in *Proceedings of the 18th International Conference on Environmental Degradation of Materials in Nuclear Power Systems – Water Reactors*, 2019, pp. 1979–1993.
- [14] M. Ahonen *et al.*, ‘Effect of Thermal Aging on Fracture Mechanical Properties and Crack Propagation Behavior of Alloy 52 Narrow-Gap Dissimilar Metal Weld’, in *Proceedings of the 18th International Conference on Environmental Degradation of Materials in Nuclear Power Systems – Water Reactors*, 2019, pp. 1949–1963.
- [15] M. Ahonen, R. Mougnot, S. Lindqvist, T. Sarikka, P. Nevasmaa, and H. Hänninen, ‘Fracture mechanical and microstructural characterization of narrow-gap safe-end dissimilar metal weld’, presented at the Baltica X, Helsinki-Stockholm, Jun. 2016, p. 16.
- [16] P. Joly, M. Yescas, and E. Keim, ‘Fracture Toughness in the Ductile-Brittle Transition and Thermal Ageing Behavior of Decarburized Heat Affected Zone of Alloy 52 Dissimilar Metal Welds of Nuclear Components’, in *Volume 6A: Materials and Fabrication*, Anaheim, California, USA, Jul. 2014, doi: 10.1115/PVP2014-29044.
- [17] W. C. Oliver and G. M. Pharr, ‘Measurement of hardness and elastic modulus by instrumented indentation: Advances in understanding and refinements to methodology’, *J. Mater. Res.*, vol. 19, no. 1, pp. 3–20, Jan. 2004, doi: 10.1557/jmr.2004.19.1.3.
- [18] F. Mas, C. Tassin, F. Roch, M. Yescas, P. Todeschini, and Y. Bréchet, ‘Growth Morphologies and Primary Solidification Modes in a Dissimilar Weld between a Low-Alloy Steel and an Austenitic Stainless Steel’, *Metals*, vol. 8, no. 4, p. 284, Apr. 2018, doi: 10.3390/met8040284.

- [19] E. Pickering and H. Bhadeshia, ‘The Consequences of Macroscopic Segregation on the Transformation Behaviour of a Pressure-Vessel Steel’, in *Volume 5: High-Pressure Technology; ASME NDE Division; Rudy Scavuzzo Student Paper Symposium*, Paris, France, Jul. 2013, doi: 10.1115/PVP2013-97097.
- [20] C. Naudin, ‘Modélisation de la ténacité de l’acier de cuve REP en présence de zones de ségrégation’, PhD thesis, Ecole des Mines de Paris, Paris, France, 1999.
- [21] A. Andrieu, ‘Mécanismes et modélisation multi-échelle de la rupture fragile trans- et intergranulaire des aciers pour réacteurs à eau sous pression, en lien avec le vieillissement thermique’, PhD thesis, Ecole des Mines de Paris, Paris, France, 2013.
- [22] M. H. Lewis and B. Hattersley, ‘Precipitation of M₂₃C₆ in austenitic steels’, *Acta Metall.*, vol. 13, no. 11, pp. 1159–1168, Nov. 1965, doi: 10.1016/0001-6160(65)90053-2.